

Collisionless shock in a laser-produced ablating plasma

A. R. Bell, P. Choi, A. E. Dangor, O. Willi, and D. A. Bassett

Blackett Laboratory, Imperial College, Prince Consort Road, London, SW7 2BZ United Kingdom

C. J. Hooker

Rutherford Appleton Laboratory, Chilton, Didcot, Oxfordshire OX11 0QX, United Kingdom

(Received 26 February 1988)

We describe experiments which throw light on the physics of high-Mach-number electrostatic shocks. A planar carbon target is irradiated with an 18-nsec laser pulse at a wavelength of $1.05 \mu\text{m}$ with an energy of 100–200 J. Carbon plasma ablates supersonically from the solid target at a velocity of $6 \times 10^7 \text{ cm sec}^{-1}$. A spherical carbon obstacle is placed in the ablating plasma at a distance of around 1 mm from the primary target where the density is $10^{18} \text{ electrons cm}^{-3}$. The density structure of the plasma is probed by interferometry and schlieren photography, and shows a density jump which can be interpreted as a bow shock in a plasma flowing with a Mach number of around 2.2. Measurements of magnetic field imply a plasma β ($8\pi nkT/B^2$) in excess of 100. The shock thickness is occasionally very thin (about $10 \mu\text{m}$), but more usually $50 \mu\text{m}$. In either case the shock thickness is much smaller than the electron and ion Coulomb mean free paths.

I. INTRODUCTION

Shock fronts are known to occur in the collisionless plasmas of the solar wind.¹ The magnetic field in the solar wind is relatively strong with an energy density comparable with the kinetic ($0.5\rho v^2$) and thermal ($1.5nkT$) energy densities.² The magnetic field plays a major role in energy dissipation since it couples together interstreaming plasmas. There is strong evidence that interactions between collisionless plasmas moving with supersonic velocities are relatively common in astrophysical plasmas outside the solar system, especially those associated with objects such as supernova remnants and active galaxies which experience a dramatic energy release.³ Although direct measurements are not possible, it is thought that shock fronts must form in such circumstances and that the Mach number of these shocks may exceed 100 (Ref. 3). The preshock energy density of the magnetic field in such plasmas is very low relative to the kinetic energy density. Even after compression in the shock, the magnetic field is too weak to be dynamically important unless amplified by turbulent processes. These nonmagnetic shocks are poorly understood, mainly because they are comparatively rare in plasmas accessible to spacecraft and difficult to produce in the laboratory, but also because theoretical work has been unable to identify a mechanism which can sustain an electrostatic shock other than at relatively low Mach number. Computer simulations have suggested that unmagnetized interstreaming plasmas do not interact above a critical Mach number $M_c = 1.6$ (Ref. 4), although M_c may be higher.⁵ This agrees with previous experiments in laser-produced plasmas.^{6,7,8} However, Eiselevich and Fainshtein⁹ have found an electrostatic interaction between oppositely directed plasma beams at densities 10^7 cm^{-3} . They find that a shock forms when the Mach number is less than 2.5–3, and that the transition thickness is around 20 D lengths.

Here we describe an experiment to investigate a collisionless shock formed by placing a solid obstacle in the path of the plasma abating from a laser-irradiated solid target (Fig. 1). An advantage of this method is that the time available for shock initiation is limited only by the

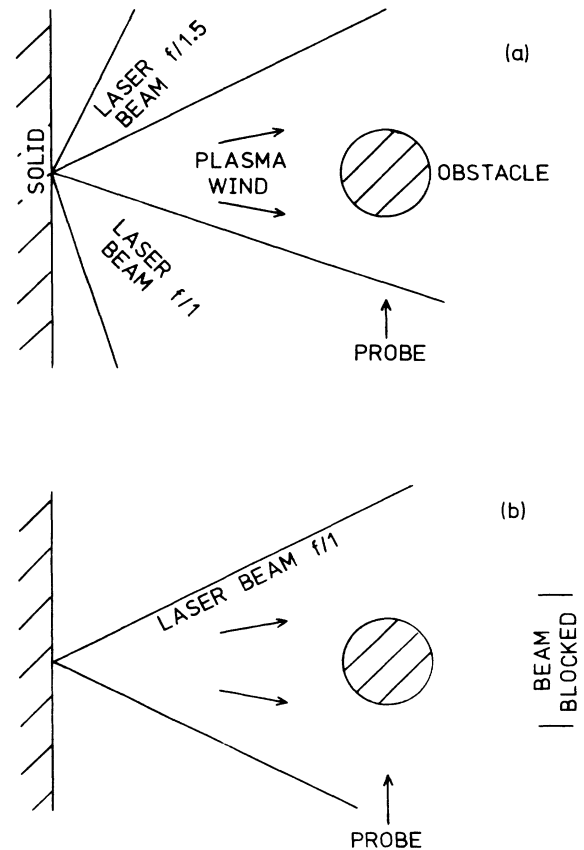


FIG. 1. Geometry of experiment (a) two-beam irradiation and (b) one-beam irradiation.

duration of the laser pulse. Thus a steady-state bow shock around the obstacle is possible. This gives maximum opportunity for the triggering of nonlinear dissipation processes, which numerical simulations suggest are not easily instigated.^{4,5} The previous laser-plasma shock experiments mentioned above have looked for a "snow-plough" interaction between the leading edge of an expanding ablated plasma and a low-density background plasma in which any possible shock is only short lived. An interaction was only found when induced by collisions^{7,10} or magnetic field.⁶

II. THE EXPERIMENTAL ARRANGEMENT

The experiments were performed using two distinct geometrical arrangements of the irradiating laser beams. In the first [Fig. 1(a)], two beams of the Vulcan laser¹¹ were overlapped on a large planar carbon target. The two beams were focused by $f/1$ and $f/1.5$ lenses, respectively, with the beam axes at right angles. The obstacle, typically $250\ \mu\text{m}$ in diameter, was placed symmetrically between the beams, 1 mm in front of the target. At this position the obstacle was outside the laser beam paths. In the second arrangement [Fig. 1(b)], only one beam is used, focussed by an $f/1$ lens. The obstacle was placed on the beam axis, and was shielded from direct laser irradiation by a blocking circular disc placed in the beam. The laser pulse was approximately Gaussian with a full width at half maximum of 18 nsec. The laser beams were brought to a focus on the surface of the target to give maximum irradiance. Each beam delivered up to 120 J on target giving an irradiance of $7 \times 10^{13}\ \text{W cm}^{-2}$ for a focal spot of $50\text{-}\mu\text{m}$ diameter as measured with a x-ray pinhole camera. When to beams were used, it was not possible in practice to overlap them accurately on target.

The plasma ablating from the primary target interacts with the spherical obstacle. The resulting density structures were viewed by a schlieren system, illuminated by a 622-nm probe beam obtained by Raman-shifting a frequency-doubled $1\text{-}\mu\text{m}$ laser beam. The Raman-shifted pulse length was 20–30 psec. The probe pulse was timed to arrive 5 nsec after the peak of the main irradiating pulse producing the plasma, but this delay was variable due to jitter in the laser system. The relative delay was monitored for most laser shots. The schlieren optics had a magnification of approximately 20. A number of different schlieren stops were used. The clearest results were obtained with a knife-edge sensitive to density gradients [$\text{grad}(\rho)$] directed parallel to the plasma flow. The most comprehensive results were obtained with a circular stop which gives sensitivity to gradients in all directions. The schlieren was sensitive to electron density gradients with $\int \nabla_{\perp} n_e dz > 4 \times 10^{17}\ \text{cm}^{-3}$, where the integration is along the probe ray path and $\nabla_{\perp} n_e$ is the electron density gradient perpendicular to the ray path.

The magnetic field was probed with single turn induction coils with diameters between 0.5 and 1 mm. The coils were electrically screened and insulated in epoxy resin. These were placed to one side of the obstacle. A wider range of coil positions was possible when the obstacle was removed. The credibility of the signal from the

coil was tested by rotating the coil through 180° and verifying that the signal was reversed.

The density structure was also probed by interferometry. For this the schlieren probe beam was used. The interference fringes were produced by separating the probe beam into two orthogonal polarizations after the plasma. The reader is referred to Benattar *et al.*¹² for a description of this technique.

III. RESULTS

Figure 2(a) is a schlieren image of the interacting plasma obtained with a knife-edge stop in the two-beam arrangement [Fig. 1(a)] with a total laser energy of 200 J. It shows a clearly defined density jump stretching over a distance of 1 mm on both sides of the obstacle in a pattern consistent with a bow shock forming around the obstacle. The width of the density jump is around 50–100 μm in the wings. The angle at which the wings spread away from the obstacle was reproducible between similar laser shots, although a shock was not detected on every occasion. Immediately in front of the obstacle the schlieren image is confused by the large density gradient leading up to solid density at the obstacle surface. This is generated by slow ablation of plasma from the obstacle due to thermal conduction from the surrounding hot plasma and irradiation by laser light reflected from the primary target.

The shock is at its strongest when the shock normal is parallel to the plasma flow, i.e., directly in front of the obstacle. As a means of separating the shock from the obstacle, some laser light was allowed to fall on the obstacle by reducing the size of the beam block in the one-beam experimental arrangement [Fig. 1(b)]. The laser irradiation causes the formation of an extended plasma atmosphere around the obstacle, thus producing an effectively larger and less dense obstacle for the plasma wind to interact with. Figure 2(b) is the resulting image using a circular schlieren stop which allows detection of density gradients in all directions. The plasma ablating from the obstacle can be seen clearly, bounded in front by a sharp density jump which is well separated from the dense obstacle. Plasma can also be seen ablating from the primary target.

When a circular schlieren stop is used, the density structure can be seen in greater detail. Figure 2(c) is one such image showing a second density gradient behind the main transition. This must be a rarefaction wave because it is never seen with a knife-edge stop orientated to detect positive density gradients.

The induction coil used to measure magnetic field was placed approximately 1 mm to the side of the obstacle and at the same distance from the primary target. The magnetic field typically rises monotonically to 15 kG during the laser pulse (18 nsec), rises further to a maximum of 25 kG after 30 nsec, and then decays again to zero. The calculated response time of the coil is 0.02 nsec.

The velocity of the ablating plasma was measured by a Faraday cup at a distance of 45 cm from the target. Most of the ions arrive with a velocity of around $6 \times 10^7\ \text{cm sec}^{-1}$, and only a very small fraction arrive with ve-

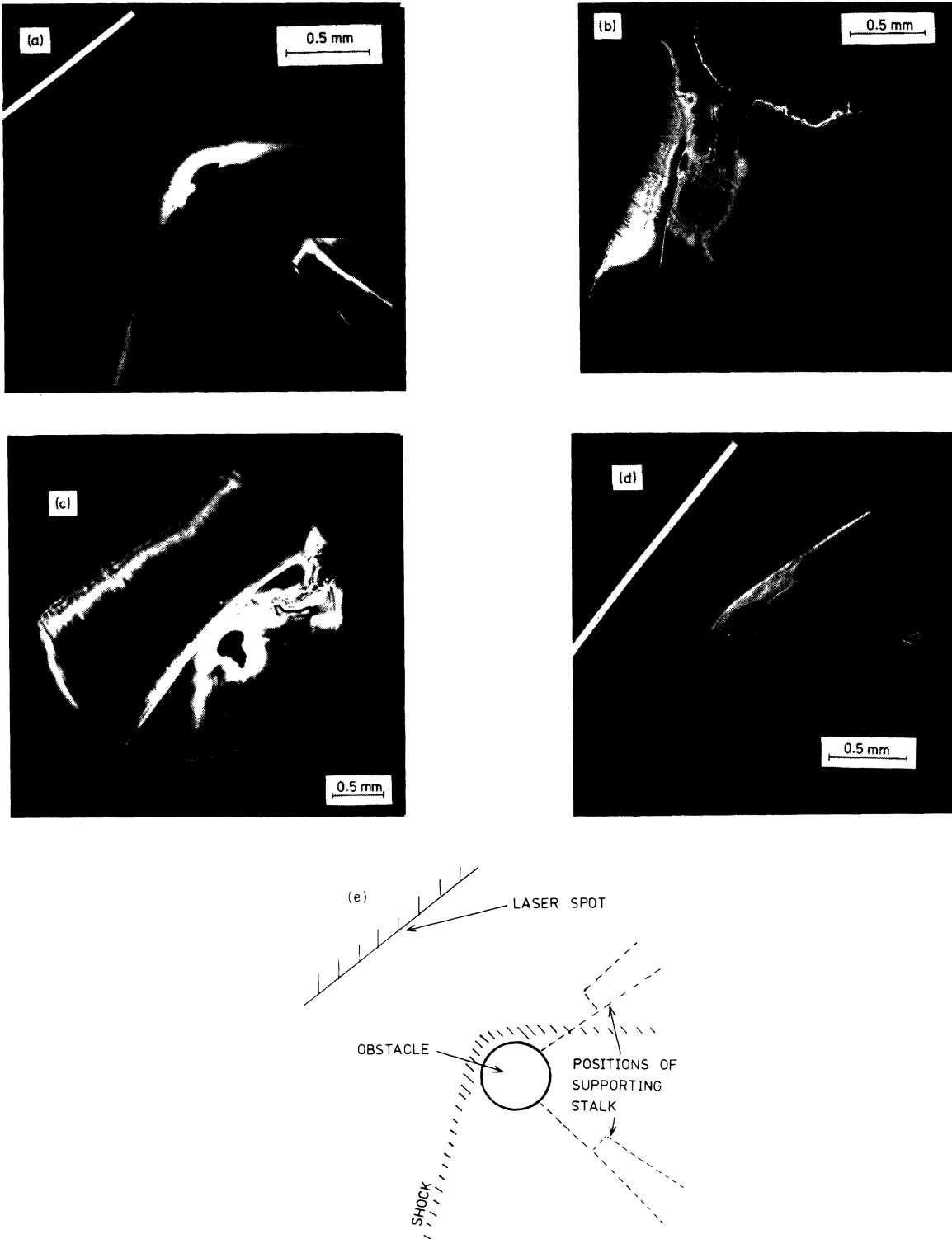


FIG. 2. Schlieren images of the ablating plasma interacting with the obstacle. (a) Two-beam irradiation of the primary target (visible at the top left), viewed with a knife-edge schlieren stop. Each of the two beams delivered approximately 100 J in tight focus. (b) Part of the laser beam was allowed to irradiate, and hence ablate the outer surface of the obstacle giving a large effective obstacle of low density. Single-beam irradiation with a circular schlieren stop. (c) Circular-stop in single-beam geometry, showing density decompression behind the shock. (d) Knife-edge stop in single-beam geometry with partial irradiation of the obstacle. This is an example of a thin shock. (e) The positions of the primary target, the obstacle, and the two orientations of the stalk supporting the obstacle. When a knife-edge stop was used, the orientation was such as to give maximum sensitivity to $\text{grad}(n_e)$ along the line between the focal spot and the obstacle.

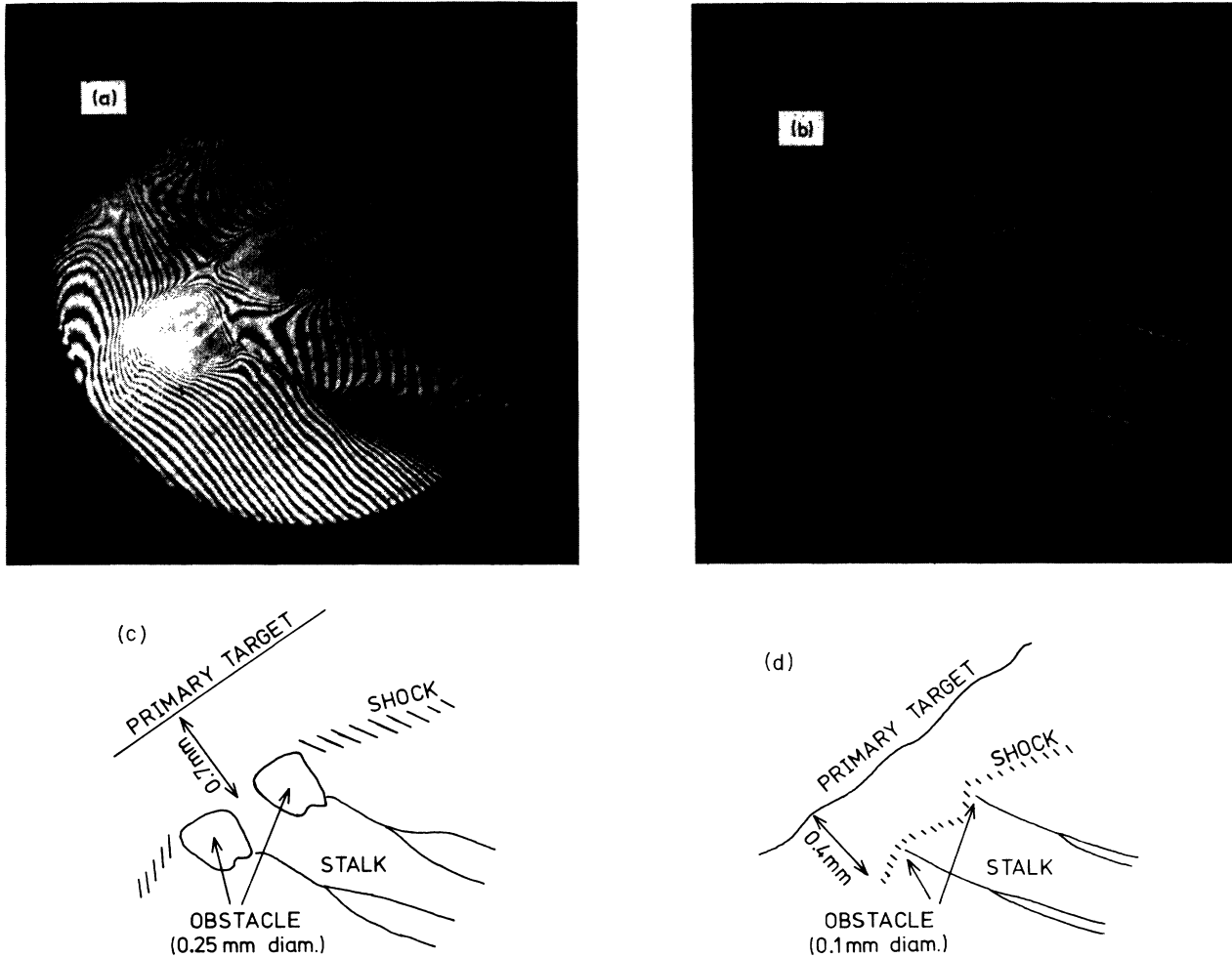


FIG. 3. Interferograms showing the double image characteristic of the Wollaston prism (a) thick shock and (b) thin shock. (c) and (d) show the corresponding positions of primary target, obstacle, and stalk.

locities less than 4×10^7 cm sec $^{-1}$. These velocities did not vary greatly between one- and two-beam arrangements.

There is evidence that the density transition occurs with two different thicknesses. Figure 2(d) shows a thin transition of around $10 \mu\text{m}$, and it is not clear that a thinner transition could be resolved by our instruments. The thin transition occurs less frequently than the thick transition.

Figure 3 shows interferograms of the density structure around the obstacle. The interferometer arrangement which used a Wollaston prism gives rise to a double image. The distance between the obstacle and the target has been shortened in order to give the higher density needed to give fringe shifts large enough to be measurable. The density transition can be seen where the fringes follow a dog-leg pattern. The density transition is sharper in Fig. 3(b) than in Fig. 3(a), which is consistent with the differing thicknesses seen with schlieren. Figure 4 is a plot of electron density, with a contour interval of 1.4×10^{18} electrons cm $^{-3}$, calculated by Abel inversion of the data in Fig. 3(a) which has a thicker jump. Following

the line superimposed on the contour plot, the plot shows a density jump A over a distance of $30\text{--}50 \mu\text{m}$, followed by a density decrease B , and a subsequent recompression C . There is no clear distinction between the thickness of the original density jump and the scale of the subsequent rarefaction and recompression.

Interferograms of the plasma ablating from the target in the absence of an obstacle show an approximate $1/r^2$ variation in the plasma flow away from the laser spot, with an electron density of about 10^{18} cm $^{-3}$ at a distance of 1 mm from the target.

IV. MACH NUMBER

For a bow shock in a uniform wind, the asymptotic angle of the wings of the shock is $\sin^{-1}(1/M)$ where M is the relevant Mach number of the flow onto the obstacle.¹³ In our case the plasma flow is divergent and we obtain an estimate of the Mach number by a two-dimensional (2D) hydrodynamic simulation of the interaction between a plasma flowing radially away from the laser focal spot and the obstacle. Cylindrical symme-

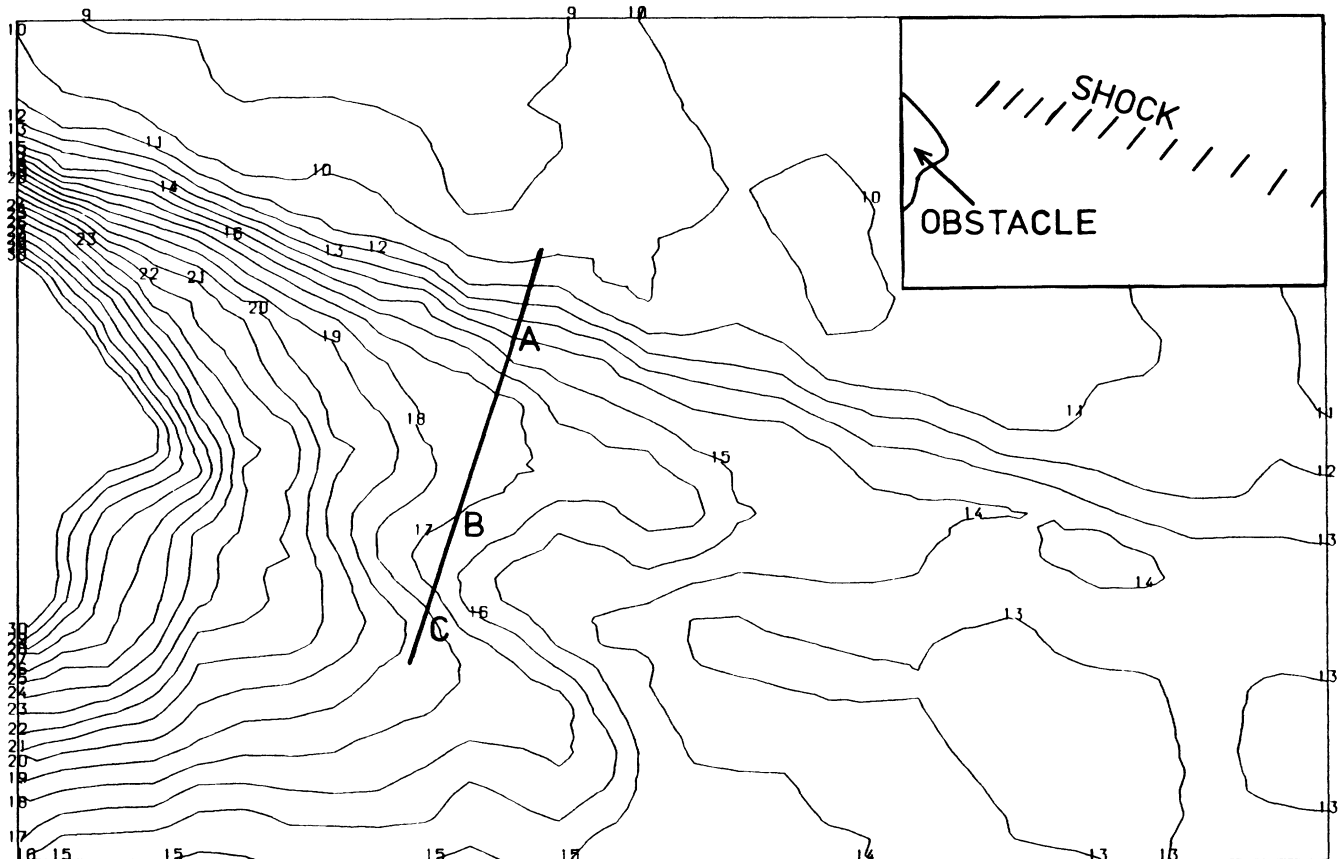


FIG. 4. Electron density contours derived by Abel inversion of the interferogram of the data in Fig. 3(a). The contour interval is 1.4×10^{18} electrons cm^{-3} . The size of the box is 0.65×0.43 mm².

try is assumed. The code¹⁴ includes artificial viscosity, but neglects other transport processes which is equivalent to assuming that electrons are strongly localized in space. The density gradient is calculated, and the expected schlieren image derived for comparison with the experimental data. We take $\gamma = \frac{5}{3}$ and find good agreement between experiment and simulation when the adiabatic Mach number at the obstacle is 2.2 (Fig. 5), with an

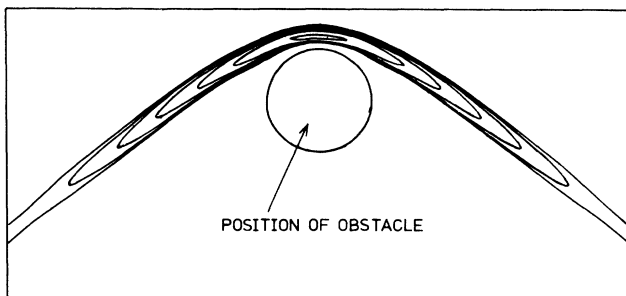


FIG. 5. Numerical simulation of schlieren image. The parameters are chosen to simulate Fig. 2(a).

equivalent isothermal Mach number of 2.8. It is notable that the simulated bow shock has the same straight wings found in the experiment. The uncertainty in the fit between simulation and experiment indicates an error of ± 0.2 in the Mach number. We investigated the effect of the neglect of transport in the code by reducing the ratio of specific heats γ to approximately represent a more isothermal plasma. This is because a reduction in the ratio of specific heats implies a larger number of internal degrees of freedom which can act as an energy sink, thereby making the plasma more isothermal. Changing γ to 1.33 or 1.2 does not significantly change the estimate of the adiabatic Mach number, although the isothermal Mach number is reduced. The Mach number was lower than that expected (4 for isothermal ablation and greater than this if the temperature falls as the density decreases) from calculations of steady spherical ablation, and may indicate the transfer of energy from the shock into the upstream plasma, possibly by shocked electrons passing back through the shock.

V. DISCUSSION

We have a sufficient set of measurements to characterize the shock parameters for the case depicted in Fig.

2(a). These parameters are set out in Table I. By interferometry in the absence of the obstacle, we know that the electron density is approximately 10^{18} cm^{-3} . Since the plasma flow is supersonic, the flow velocity at the obstacle is close to that measured by time-of-flight measurement at the wall of the target chamber, $6 \times 10^7 \text{ cm sec}^{-1}$. The adiabatic Mach number of the flow is around 2.2, implying a sound speed of $2.7 \times 10^7 \text{ cm sec}^{-1}$. Assuming that the plasma is fully ionized, the sound speed implies a preshock electron temperature of 800 eV. These parameters then define the various Coulomb mean free paths.¹⁵ A carbon ion with a velocity of $6 \times 10^7 \text{ cm sec}^{-1}$ passing through a plasma with an electron density of 10^{18} cm^{-3} and a temperature of 800 eV, has a mean free path of 20 mm for collision with other ions and a mean free path of the order of thousands of mm for energy loss to electrons. The mean free path for electrons is more difficult to estimate because of its strong dependence on the poorly determined electron velocity. However, electrons at the estimated preshock temperature of 800 eV have mean free paths (for an electron with energy $3kT/2$) of 1.8 mm for angular scattering by ions and 9 mm for electron-electron energy exchange. Electrons heated by the shock will have larger velocities and longer mean free paths. All these mean free paths are much larger than the transition thickness (0.05 mm). The shortest of the mean free paths (electron-ion angular scattering) does not transfer energy between particles and is negligible for momentum transfer because the electron mass is small compared with the ion mass.

The magnetic field is typically 10 kG at the time of probing, implying an upstream β of 300. Clearly the upstream magnetic pressure is too small to be important dynamically. However, the gyroradius of a 800-eV electron is only 0.07 mm, which is comparable with the shock thickness. Hence the magnetic field may be restricting the motion of electrons on this scale. Quest¹⁶ has shown numerically that a relatively weak magnetic field (Alfvén Mach number up to 60) can be important in

a shock, but his shock thickness (many times the ion collisionless skin depth c/ω_{pi}) is much larger than ours. The gyroradius of an ion with velocity $6 \times 10^7 \text{ cm sec}^{-1}$ is 12 mm and ion gyration is therefore unimportant. It should be noted that the magnetic field is measured in unshocked plasma, and it is possible that much larger self-generated microscopic fields are present in the shock.

The density structure is three dimensional (3D), but only the outer edge of the 3D cone is detected by schlieren due to integration along the cone surface giving greater angular refraction of the probe beam. It is possible that 3D effects cause the density transition to appear larger than is actually the case. However, limb brightening would then be expected to give a sharper edge to the front of the transition than that observed. Moreover, the Abel inversion of the interferogram (Fig. 4) would reveal a thinner transition, which is similarly not observed. It is also unlikely that the image is smeared by time integration since the density structure would have to move at a velocity of $2 \times 10^8 \text{ cm sec}^{-1}$ (three times the plasma wind velocity) to explain the observed transition thickness. We therefore think that the width of the schlieren image of the transition represents its true width.

The thickness of the density transition is usually taken as an indication of the dissipation mechanism. Ideally, most information can be obtained from the scaling of the thickness with density and shock velocity, but we had insufficient diagnostic sensitivity to scan the necessary range of parameters. However, it is still profitable to compare our transition thickness with important plasma parameters. Taking the parameters enumerated at the beginning of this section, the Debye length is $0.2 \mu\text{m}$ and the collisionless skin depth is $5 \mu\text{m}$. In comparison our "thick" transitions have a thickness of around $50 \mu\text{m}$, and our "thin" transitions around $10 \mu\text{m}$. The thick transitions have a thickness which is around 250 times the Debye length which implies that they are not purely electrostatic. On the other hand, their thickness is around $10c/\omega_{pe}$, which is the thickness often found for a

TABLE I. Shock parameters.

Preshock electron density	10^{18} cm^{-3}
Shock velocity	$6 \times 10^7 \text{ cm sec}^{-1}$
Acoustic Mach number	2.2
Sound speed	$2.7 \times 10^7 \text{ cm sec}^{-1}$
Preshock electron temperature	800 eV
Magnetic field	10 kG
Alfvén Mach number	40
Upstream β	300
Mean free path (MFP) for ion-ion collision	20 mm
MFP for ion energy loss to electrons	2000 mm
Preshock MFP for electron scattering by ions	1 mm
Preshock MFP for electron-electron energy exchange	6 mm
Ion gyroradius	12 mm
800-eV electron gyroradius	0.07 mm
Upstream Debye length	0.0002 mm
Upstream collisionless skin depth	0.005 mm
Shock thickness	0.01–0.05 mm

perpendicular magnetic shock. This may suggest that the shock is magnetic in character, in which case the magnetic field must be produced by processes within the shock. This would be consistent with rare observations of weakly magnetic shocks in the solar wind.¹⁷ Our thin transition has a thickness which is around 50 times the Debye length, and hence we cannot rule out the possibility that the shock is electrostatic in nature. This would be qualitatively in agreement with the experiments of Eselevich and Fainshtein,⁹ mentioned in our Introduction, which show an electrostatic density jump on the scale of 20 D lengths.

VI. CONCLUSIONS

We have shown that a laser-produced ablating plasma, when encountering a solid obstacle, forms a density structure which can be interpreted as a collisionless bow shock. The magnetic field in the preshock plasma is weak (~ 10 kG) such that the plasma β is around 300 and the Alfvén Mach number is around 40. The acoustic Mach number is 2.2 which is lower than expected and may indicate energy leakage into the upstream plasma. The shock thickness is occasionally $\sim 10 \mu\text{m}$ ($\sim 50\lambda_D$) but is more usually $\sim 50 \mu\text{m}$ ($\sim 10c/\omega_{pe}$).

-
- ¹D. A. Tidman and N. A. Krall, *Shock Waves in Collisionless Plasmas* (Wiley, New York, 1971).
²E. W. Greenstadt and R. W. Fredricks, in *Solar System Plasma Physics*, edited by L. J. Lanzerotti, C. F. Kennel and E. N. Parker (North-Holland, Amsterdam, 1979), Vol. III, Chap. III.
³C. F. McKee and D. J. Hollenbach, *Ann. Rev. Astron. Astrophys.* **18**, 219 (1980).
⁴R. J. Mason, *Phys. Fluids* **15**, 845 (1972).
⁵D. Biskamp, *Nucl. Fusion* **13**, 719 (1973).
⁶A. Y. Cheung, R. R. Goforth, and D. W. Koopman, *Phys. Rev. Lett.* **31**, 429 (1973).
⁷T. P. Wright, *Phys. Rev. Lett.* **28**, 268 (1972).
⁸P. T. Rumsby, J. W. M. Paul, and J. Beaulieu, *Bull. Am. Phys. Soc.* **16**, 1191 (1971).
⁹V. G. Eselevich and V. G. Fainshtein, *Fiz. Plasmy* **10**, 538 (1984) [*Sov. J. Plasma Phys.* **10**, 313 (1984)].
¹⁰S. O. Dean, E. A. McLean, J. A. Stamper, and H. R. Griem,

- Phys. Rev. Lett.* **27**, 487 (1971); **29**, 569 (1972).
¹¹I. N. Ross, M. S. White, J. E. Boon, D. Craddock, A. R. Damerell, R. J. Day, A. F. Gibson, P. Gottfeldt, D. J. Nicholas, and C. J. Reason, *IEEE J. Quant. Electron* **QE-17**, 1653 (1981).
¹²R. Benattar, C. Popovics, and R. Sigel, *Rev. Sci. Instrum.* **50**, 1583 (1979).
¹³L. D. Landau and E. M. Lifshitz, *Fluid Mechanics* (Pergamon, New York, 1959).
¹⁴R. A. Gentry, R. E. Martin, and B. J. Daly, *J. Comput. Phys.* **1**, 87 (1966).
¹⁵L. Spitzer, *Physics of Fully Ionized Gases* (Interscience, New York, 1956).
¹⁶K. B. Quest, *J. Geophys. Res.* **91(A8)**, 8805 (1986).
¹⁷V. Formisano, C. T. Russell, J. D. Means, E. W. Greenstadt, F. L. Scarf, and M. Neugebauer, *J. Geophys. Res.* **80**, 2013 (1975).

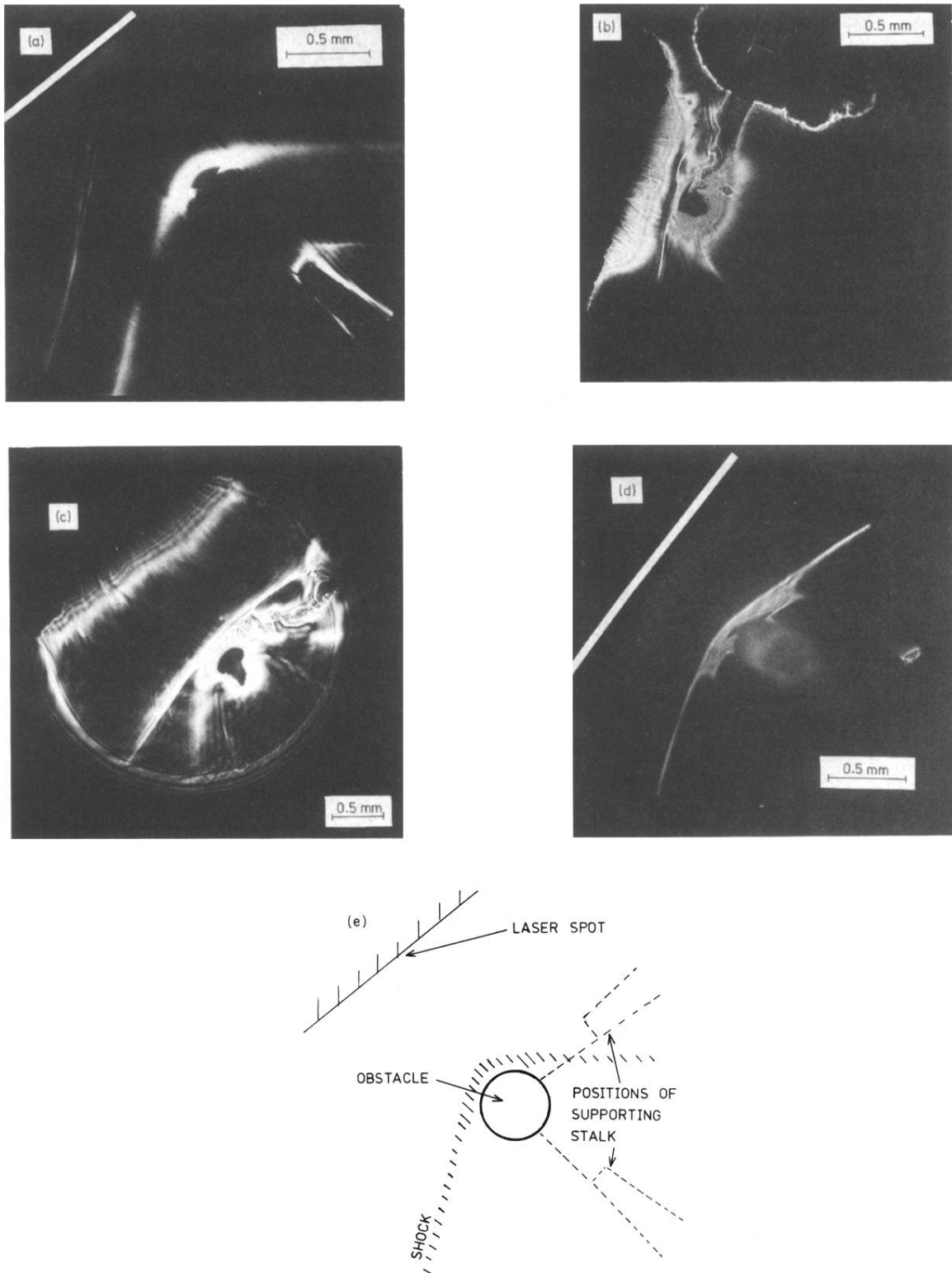


FIG. 2. Schlieren images of the ablating plasma interacting with the obstacle. (a) Two-beam irradiation of the primary target (visible at the top left), viewed with a knife-edge schlieren stop. Each of the two beams delivered approximately 100 J in tight focus. (b) Part of the laser beam was allowed to irradiate, and hence ablate the outer surface of the obstacle giving a large effective obstacle of low density. Single-beam irradiation with a circular schlieren stop. (c) Circular-stop in single-beam geometry, showing density decomposition behind the shock. (d) Knife-edge stop in single-beam geometry with partial irradiation of the obstacle. This is an example of a thin shock. (e) The positions of the primary target, the obstacle, and the two orientations of the stalk supporting the obstacle. When a knife-edge schlieren stop was used, the orientation was such as to give maximum sensitivity to $\text{grad}(n_e)$ along the line between the focal spot and the obstacle.

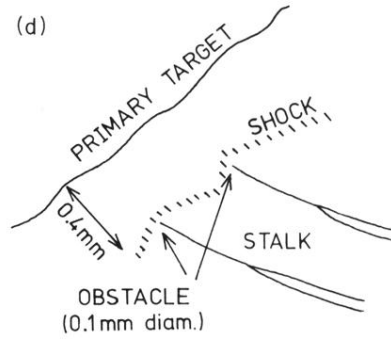
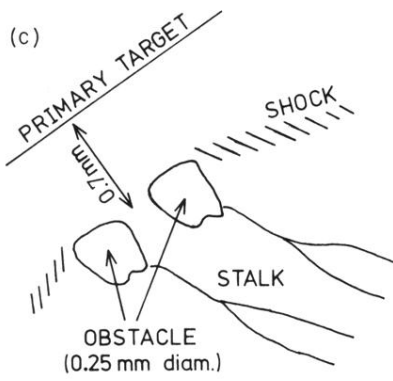
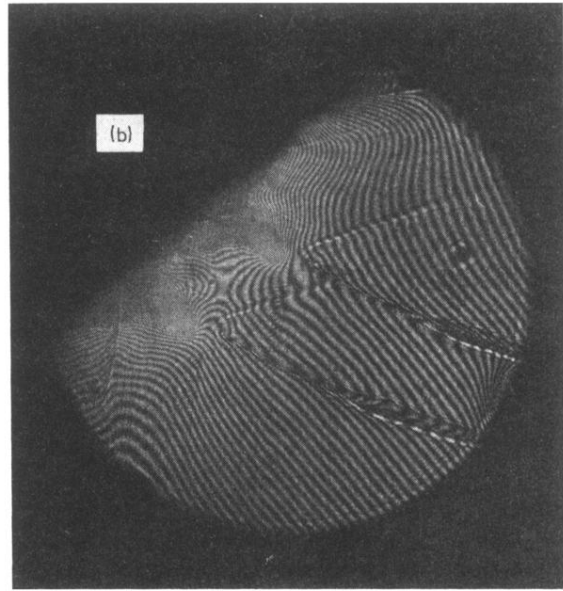
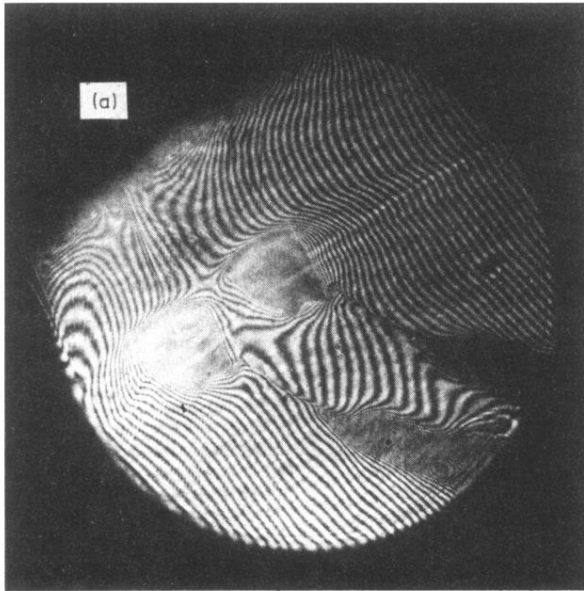


FIG. 3. Interferograms showing the double image characteristic of the Wollaston prism (a) thick shock and (b) thin shock. (c) and (d) show the corresponding positions of primary target, obstacle, and stalk.